74th International Astronautical Congress (IAC), Baku, Azerbaigian, 2-6 October 2023.

IAC-23,B4,8,5,x79559

Design, Analysis and Validation of the ADCS for the LUMIO mission

Antonio Rizza[1], Felice Piccolo[2], Paolo Panicucci[3], Salvatore Borgia[4], Giorgio Saita[5], Giovanni Fumo[6], Gianmario Merisio[7], Lorenzo Provinciali[8], Francesco Topputo[9]

The LUnar Meteoroid Impact Observer (LUMIO) is a 12U deep-space CubeSat mission with the goal of observing, quantifying, and characterizing the meteoroid impacts on the lunar farside. The spacecraft is designed to operate on a quasi-halo orbit at the Earth-Moon L2 Lagrangian point to complement ground-based observation of our natural satellite. This paper presents the relevant requirements, the design choices, and the analysis performed to validate the CubeSat ADCS design. An overview of the subsystem is provided illustrating the final configuration adopted. High-fidelity numerical simulations are performed using state-of-the-art in-house tools to assess the performances of the system in different operative scenarios from release to demise in terms of pointing accuracy, momentum budget and total impulse. Monte Carlo simulations are also performed to statistically assess the robustness of the design to uncertainties. The presented design is developed during the Phase B study under ESA contract. The consortium is led by the Deep-space Astrodynamics Research and Technology (DART) group at Politecnico di Milano, with the Argotec team responsible for the system design and platform manufacturing.

1 Introduction

The Earth-Moon system is constantly bombarded by meteoroids of different sizes. Fragments of asteroids, comets, and major celestial bodies continuously impact our planet and its natural satellite. The modeling of Solar System meteoroids can provide valuable information about the spatial distribution of objects near the Earth-Moon system and it can be used to predict the degradation of spaceborne equipment and to forecast large impacts on Earth [1]. Meteoroid flux models have relied on Earth-based observations of meteor showers and lunar flashes due to meteoroid impacts. Unfortunately, Earth-based observations as they are constrained by geometrical, illumination, and meteorological conditions, which limit the possibility to detect impacts. A Moon-based observatory would overcome these limitations and increase the quality and quantity of meteoroid impacts detection, improving current meteoroid models. In this context, the Lunar Meteoroid Impacts Observer (LUMIO) mission has been designed and is currently in Phase B under ESA funding [2]. LUMIO is a CubeSat mission to a halo orbit at Earth-Moon L2 that shall observe, quantify, and characterize meteoroid impacts on the Lunar farside by detecting their flashes, complementing Earth-based observations on the Lunar nearside, to provide global information on the Lunar Meteoroid Environment and contribute to Lunar Situational Awareness [3, 4]. Moreover, the LUMIO mission foresees to enable key technologies on orbit to enable interplanetary CubeSats and their operations, such as the demonstration of the miniaturized propulsion system and the miniaturized payload. Furthermore, a technological experiment is foreseen to demonstrate the feasibility of autonomous vision-based navigation at the Moon [5].

In this work, the ADCS subsystem is presented, illustrating the relevant requirements, the current configuration and the main analyses conducted for the Phase B study. The analyses are focused on the validation of the system and AOCS design, particularly in terms of actuators sizing and configuration. The rest of the paper is structured as follows. Sec. 2 gives an overview of the current LUMIO mission design. Sec. 3 presents the current configuration of the AOCS system, and Sec. 4 illustrates the models used for numerical simulations. Then, Sec. 5 describes the relevant ADCS analyses, while Sec. 6 gives some final remarks and concludes the paper.

[1]PhD Student, Department of Aerospace Science and Technology, Politecnico di Milano, Via La Masa 34, 20156, Milano, Italy, antonio.rizza@polimi.it
[2]PhD Student, Department of Aerospace Science and Technology, Politecnico di Milano, Via La Masa 34, 20156, Milano, Italy; felice.piccolo@polimi.it
[3]Assistant Professor, Department of Aerospace Science and Technology, Politecnico di Milano, Via La Masa 34, 20156, Milano, Italy, paolo.panicucci@polimi.it
[4]PhD Student, Department of Aerospace Science and Technology, Politecnico di Milano, Via La Masa 34, 20156, Milano, Italy, salvatore.borgia@polimi.it
[5]System Engineer, Argotec, Via Cervino, 52, 10155, Torino, Italy, giorgio.saita@argotecgroup.com
[6]System Engineer, Argotec, Via Cervino, 52, 10155, Torino, Italy, giovanni.fumo@argotecgroup.com
[7]PostDoc Researcher, Department of Aerospace Science and Technology, Politecnico di Milano, Via La Masa 34, 20156, Milano, Italy, salvatore.borgia@polimi.it
[8]System Engineer, Argotec, Via Cervino, 52, 10155, Torino, Italy, lorenzo.provinciali@argotecgroup.com
[9]Full Professor, Department of Aerospace Science and Technology, Politecnico di Milano, Via La Masa 34, 20156, Milano, Italy, francesco.topputo@polimi.it

Tab. 1: Driving ADCS system requirements.

ID	Requirement text
ADC.010	The ADCS shall be able to de-tumble the spacecraft from tip-off rates of 10 deg/s on each axis down to at least 1.5 deg/s on each axis.
ADC.011	The spacecraft shall execute an autonomous detumbling after orbit injection to be completed within 20 minutes.
ADC.032	The spacecraft shall provide an Absolute Performance Error (APE) lower than 0.2 deg half cone (TBC) (99.73% probability and 95% confidence level) when performing DTE communication.
ADC.033	The spacecraft shall provide an Absolute Performance Error (APE) lower than 0.5 deg half cone (TBC) (99.73% probability and 95% confidence level) when maneuvering.
ADC.040	The spacecraft shall provide a Relative Performance Error (RPE) lower than 2.1 arcsec (99.73% probability and 95% confidence level) over 78 ms when performing science.
ADC.050	The spacecraft shall provide an Absolute Knowledge Error (AKE) lower than 72 arcsec half cone (TBC) (99.73% probability and 95% confidence level).
ADC.090	The AOCS shall be able to correct the pointing during main engine firing considering: 1) A relative thrust magnitude error of 6.1% (3-sigma) with respect to the commanded thrust level. 2) A thruster misalignment error randomly distributed within an elliptical cone of 1 deg (3-sigma). 3) A displacement of the center of mass sampled with a uniform distribution within a cylinder centered in the geometrical center of the spacecraft with radius equal to 10mm (TBC) and total height equal to 30mm (TBC).

2 The LUMIO mission

LUMIO is a CubeSat mission designed to improve our understanding of the meteroid flux impacting the Earth-Moon system [6]. Due to the tidally-locked motion of the Moon, only impacts on its near side can be detected from Earth. Therefore, LUMIO will operate on a halo orbit around the Earth-Moon L_2 Lagrange point, so that it will complement Earth-based observations by monitoring the lunar far side. Impact detections are carried out by the mission's scientific payload, the LUMIO-Cam. It consists of a narrow-angle camera with two detectors providing the possibility of observing the flashes in the visible and the near-infrared spectra. Fig. 1 illustrates the mission timeline. The spacecraft will perform a weak stability boundary (WSB) transfer to the Moon, which will last between 90 and 140 days. It will be released on the lunar transfer trajectory, where it will perform commissioning immediately after release, and then execute a series of trajectory correction manoeuvres. After the transfer, a Halo Injection Maneuver will place the spacecraft in its operative orbit. The nominal mission on the halo orbit lasts 1 year and it will end by impacting the spacecraft on the Moon.

Thanks to the almost-periodic behavior of halo orbits, two alternating operative phases are foreseen during the nominal mission [7]: the Science Cycle and the Navigation & Engineering (Nav&Eng) Cycle. The former lasts approximately 14 days and occurs when the lunar farside has the optimal illumination conditions to perform flash detection (i.e., at least half of the Moon is not illuminated). The latter is defined as the complementary of the Science Cycle, and it covers the phase during which most of the Moon is illuminated. During the Nav&Eng Cycle, LUMIO performs engineering activities (e.g., reaction wheel desaturation, communication with the Earth, station-keeping, and technological demonstration) as it cannot carry out scientific observations. A sketch of the LUMIO concept of operation is reported in Fig. 2 for the sake of completeness.

The LUMIO consortium is led by Politecnico di Milano, which is responsible for the mission analysis, AOCS/GNC analyses, optical navigation experiment and the scientific segment of the mission. The system integrator and platform provider is Argotec, which performs system level analyses and supports other design activities. The custom payload is designed by Leonardo, with a dedicated on-board payload data processing unit provided by S[&]T. The spacecraft will also be equipped with a Solar Array Drive Assembly (SADA) and X-band transponder developed by IMT. Finally, the ground segment and operations are in charge of Nautilus.

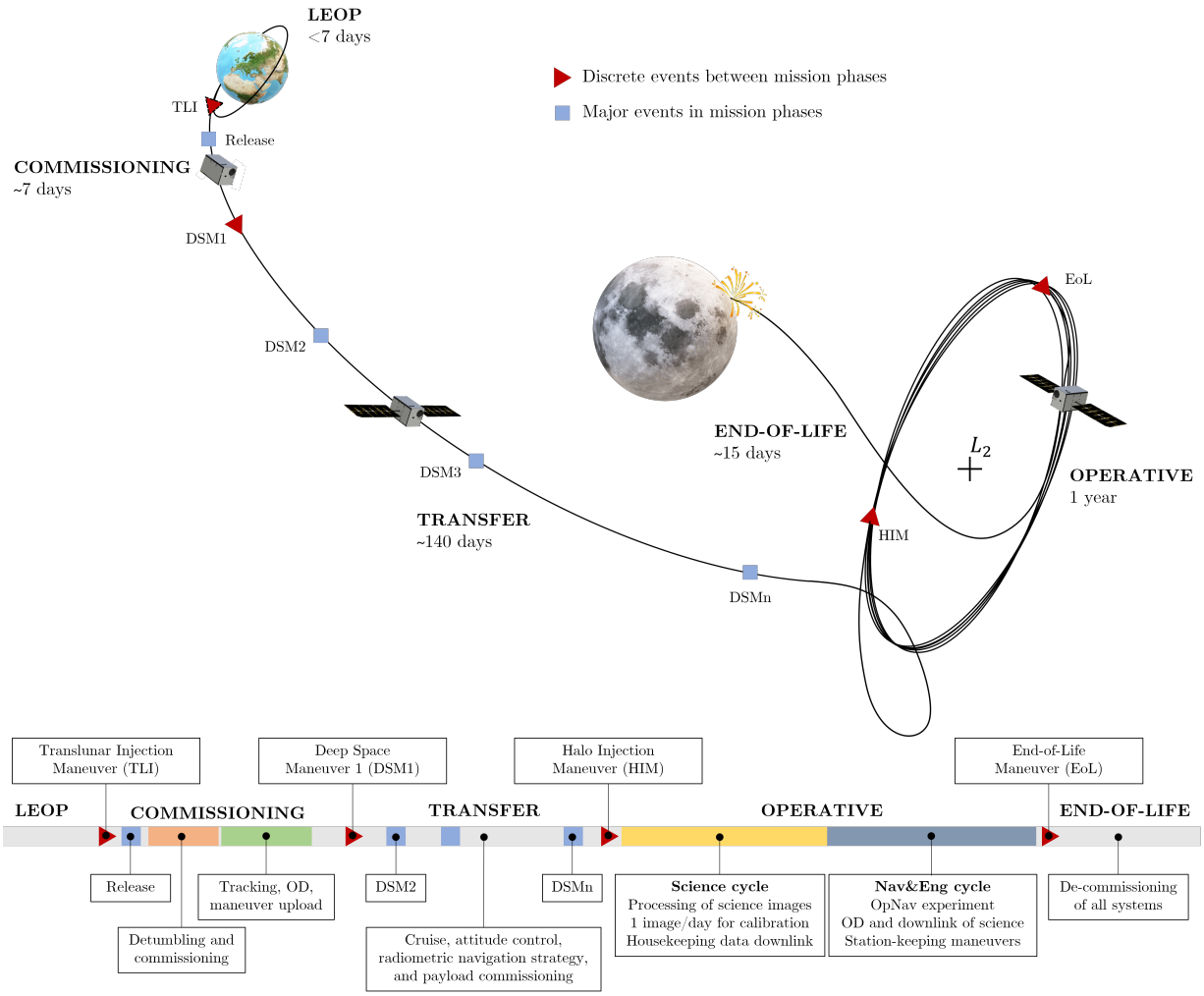

Fig. 1: LUMIO mission timeline

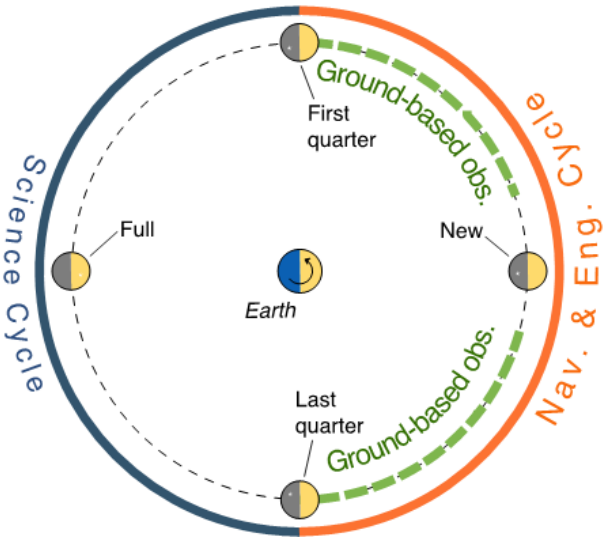

Fig. 2: LUMIO concept of operation.

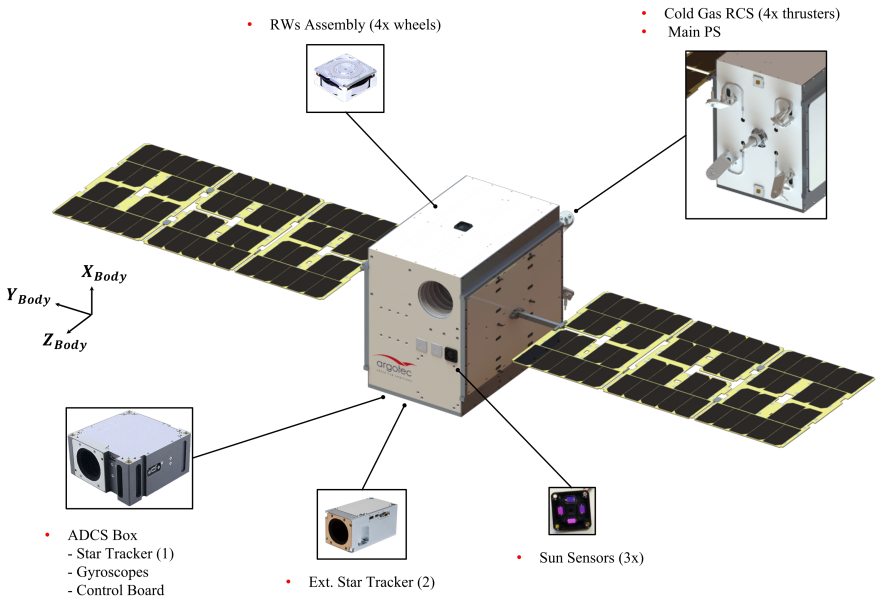

Fig. 3: LUMIO AOCS configuration

3 AOCS system description

The current configuration of the attitude and orbit control system (AOCS) is shown in Fig. 3, which also shows the LUMIO body reference frame (BRF). The AOCS is in charge of performing several operations such as pointing to the Moon to perform science and the optical navigation experiment, to the Earth to communicate with the ground station, and to the Sun as secondary pointing to ensure power generation. Moreover, station-keeping and orbital correction maneuvers must be performed to ensure the operative orbit insertion, the 1-year nominal mission on the halo orbit, and the correct end-of-life impact on the Moon. Tab. 1 reports the main requirements for the ADCS system design.

During the Science Cycle, the nominal pointing of the spacecraft is defined such that the LUMIO-Cam points towards the Moon. The remaining degree of freedom is exploited to maximize power generation. To this end, the SADA axis, i.e., the axis around which the solar panels rotate, is kept perpendicular to the Sun direction. During other mission phases a different pointing may be required, e.g. to communicate with Earth during the Nav&Eng Cycle. The LUMIO body reference frame (BRF) is defined such that the z axis points in the direction of the LUMIO-Cam, while the y axis corresponds to the SADA axis, and the x axis completes the right handed frame. The BRF axes are indicated as x_B, y_B and z_B.

The AOCS system is composed of:

1. The main propulsion system (PS), or main engine (ME), which is composed of a single thruster.
2. A reaction control system (RCS) composed of 4 thrusters.
3. A reaction wheel (RW) assembly composed of 4 wheels.
4. An ADCS box containing a star tracker, a set of gyroscopes and a control board.
5. A second star tracker in cold redundancy.
6. Three sun sensors.

The main PS performs orbital maneuvers during the whole mission. It is located on the centre of the -Z face of the CubeSat and fires in the $-z_B$ direction. It is characterized by a blowdown system with a maximum thrust of 1 N that decreases during the mission up to about 0.25 N. The RCS thrusters are positioned on the same panel as the main PS, but are mounted on a set of brackets, and the firing direction is defined by two angles, α and β, which are illustrated in Fig. 4. The RW assembly is characterized by 3 RW with a maximum momentum storage of 100 mN m s and 1 with 50 mN m s. Each of the larger wheels is aligned with one of the spacecraft body axes, while the remaining one is tilted. The RW configuration matrix is given by:

$$A_{RW} = \begin{bmatrix} 1 & 0 & 0 & -\frac{\sqrt{3}}{3} \\ 0 & 1 & 0 & -\frac{\sqrt{3}}{3} \\ 0 & 0 & 1 & -\frac{\sqrt{3}}{3} \end{bmatrix}$$

Finally, the main ST points in the $-x_B$ direction, while the redundant one is slightly tilted because of accommodation constraints.

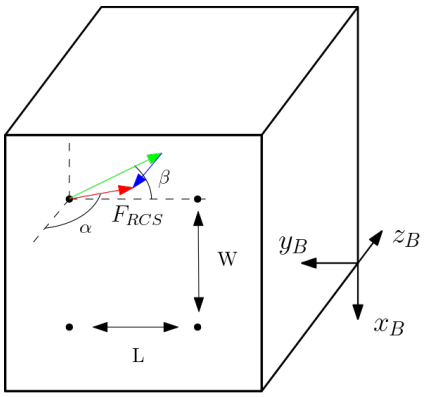

Fig. 4: Illustration of the RCS desing parameters.

4 Simulation environment

The LUMIO ADCS design is supported by high-fidelity simulations performed within the in-house designed CubeSat Orbit and GNC (CUBORG) simulation environment [8]. CUBORG is a general purpose functional engineering simulator developed in MATLAB/Simulink with three functional segments: an input dataset, a MATLAB segment and a Simulink segment. The input dataset contains all the configuration parameters required to set up the simulation together with different kind of data (e.g., kernels and shape models). The MATLAB segment is formed by a set of functions that are used to read the input parameters, set up the simulation, manage the toolbox interfaces and post-process the outputs. The Simulink segment is composed of two Simulink files: a library and a simulation model. The former contains a wide list of in-house developed models that can be used to simulate both the behavior of the environment and the spacecraft. Different levels of fidelity are available enabling for a modular simulation approach with progressively growing complexity as the design proceeds forward. The simulation model, instead, is the core of the simulator, and in turn is divided into three main sections: environment, spacecraft and output. The first two contain a pre-defined template, respectively for the environment and for the spacecraft, in which library elements can be plugged, either manually or programmatically. The output section is used to process and save selected simulation data. A detailed description of the tool and its functionalities can be found in [8]. In the following the focus is put on the models adopted for validating the design of the LUMIO ADCS.

4.1 Spacecraft dynamics

As ADCS functionalities need to be tested, only the rotational dynamics is simulated, the translational motion of the spacecraft is not integrated, but it is retrieved from SPICE kernels. The spacecraft state is therefore given by $\{q, \boldsymbol{\omega}\}$ where $q = [q_0, \mathbf{q}]^T$ is the attitude quaternion describing the rotation from the ECI-J2000 reference frame to the LUMIO BRF and $\omega = [\omega_x, \omega_y, \omega_z]^T$ is the spacecraft angular velocity expressed in the LUMIO BRF. In this paper every time that a vector is expressed in BRF the index of the reference frame is omitted. Attitude dynamics and kinematics are governed respectively by the Euler's equation (Eq. 1), and by the fundamental kinematic equation (Eq. 2).

$$\mathbf{J}\dot{\boldsymbol{\omega}} = \mathbf{J}\boldsymbol{\omega} \times \boldsymbol{\omega} + \mathbf{T}_e + \mathbf{u} \tag{1}$$

$$\dot{q} = \frac{1}{2}\boldsymbol{\Omega} q \tag{2}$$

where $\mathbf{J}$ is the inertia tensor, $\mathbf{T}_e$ and $\mathbf{u}$ are respectively the environmental and control torque acting on the spacecraft and expressed in BRF while $\boldsymbol{\Omega}$ is a matrix obtained from the spacecraft angular velocity vector as:

$$\boldsymbol{\Omega} = \begin{bmatrix} 0 & -\omega_x & -\omega_y & -\omega_z \\ \omega_x & 0 & \omega_z & -\omega_y \\ \omega_y & -\omega_z & 0 & \omega_x \\ \omega_z & \omega_y & -\omega_x & 0 \end{bmatrix} \tag{3}$$

The movement of the solar panels due to the SADA produces a variation of the spacecraft inertia. The latter is modeled as:

$$\begin{aligned} \mathbf{J} = \mathbf{J}_B + 2\mathbf{R}^T(\theta_{SADA})\mathbf{J}_{SP}^{SP}\mathbf{R}(\theta_{SADA}) + \\ + m_{SP1}\left[\mathbf{d}_{SP1}\right]_X^T\left[\mathbf{d}_{SP1}\right]_X + \\ + m_{SP2}\left[\mathbf{d}_{SP2}\right]_X^T\left[\mathbf{d}_{SP2}\right]_X \end{aligned} \tag{4}$$

combining the contributions due to the main body's inertia $\mathbf{J}_B$, the solar panel's inertia $\mathbf{J}_{SP}$ expressed in the Solar Array Reference Frame (SARF) and the Huygens–Steiner transport terms. In Eq. 4, $\mathbf{R}(\theta_{SADA})$ indicates the rotation from SARF to BRF as a function of the SADA rotation angle, m_{SPj} is the mass of jth solar panel, and $\left[\mathbf{d}_{SPj}\right]_X$ the skew-symmetric matrix obtained from the vector $\mathbf{d}_{SPj}$ that defines the jth solar panel center of mass with respect to the BRF.

Given its operative orbit, the only environmental perturbation considered on the spacecraft is the Solar Radiation Pressure (SRP), which is computed according to a flat plate model [9]. For each face of the spacecraft the force due to solar pressure is computed as:

$$\begin{aligned} \mathbf{F}_{SRP,k} = -\gamma_k \tfrac{1}{c}\tfrac{P_0}{r_{AU}^2} A_k cos(\theta_k)[(1-\rho_{s,k})\hat{\mathbf{r}}_S + \\ + 2\left(\tfrac{\rho_{d,k}}{3} + \rho_{s,k} cos(\theta_k)\right)\mathbf{n}_k] \end{aligned} \tag{5}$$

where n_f is the total number of faces, γ_k is a boolean flag different from zero when the kth face is illuminated, c and P_0 respectively the speed of light in vacuum and the solar pressure at 1 Astronomical Unit (AU), r_{AU} the

spacecraft distance from the Sun expressed in AU, A_k the area of each face, θ_k the Sun incidence angle, $\hat{\mathbf{r}}_S$ the Sun to Spacecraft unit vector expressed in body frame and $\mathbf{n}_k$ the normal to the surface. Surface materials and coatings define instead the optical properties of the face in terms of specular $\rho_{s,k}$ and diffusive $\rho_{d,k}$ reflectivity. All surfaces are assumed to be opaque in this model. The environmental torque acting on the spacecraft is then given by:

$$\mathbf{T}_e = \mathbf{T}_{SRP} = \sum_{k=1}^{n_f} \mathbf{r}_k \times \mathbf{F}_{SRP,k} \tag{6}$$

where $\mathbf{r}_k$ is the relative position of the center of pressure with respect to the spacecraft center of mass expressed in body frame. It is currently assumed that the center of pressure coincides with the geometrical centre of each CubeSat face.

4.2 Sensor models

The spacecraft carries three types of attitude sensors: Sun Sensors (SS), Star Trackers (ST) and an Inertial Measurement Unit (IMU). The SS model outputs the Sun direction $\hat{\mathbf{S}}_{SS}^{SS}(q,t,\gamma)$ in the sensor reference frame, where γ groups a set of sensor parameters. The SS measurement is given by:

$$\hat{\mathbf{S}}_{SS}^{SS} = \nu(q,t) \begin{bmatrix} \cos(\beta_{SS}+n_\beta)\cos(\alpha_{SS}+n_\alpha) \\ \cos(\beta_{SS}+n_\beta)\sin(\alpha_{SS}+n_\alpha) \\ \sin(\beta_{SS}+n_\beta) \end{bmatrix} \tag{7}$$

where $\nu(q,t)$ is a boolean variable set to 1 when the Sun is in the sensor field of view (FoV), α_{SS} and β_{SS} are the two angles giving the ideal direction of the Sun in the sensor reference frame, $n_\beta \in \mathcal{N}(0,\sigma_{cb})$ and $n_\alpha \in \mathcal{N}(0,\sigma_b)$ are the Gaussian noise in the cross-boresight and boresight direction respectively.

The ST model returns the orientation q_{ST} of the sensor with respect to the ECI-J2000 as:

$$q_{ST} = \nu_S(q,t)\nu_\omega(\omega) q_n(t) \otimes q \otimes q_{B2ST} \tag{8}$$

where $\nu_S(q,t)$ and ν_ω are boolean variables that go to zero respectively when the Sun enters the instrument FoV and when the spacecraft angular rate exceeds the ST working limit, q_n accounts for the instrument noise and q_{B2ST} is the rotation quaternion from BRF to ST frame. Noise is assumed Gaussian with a potentially different standard deviation on each axis. Note that the use of the Hamilton product, indicated by the symbol $\otimes$ in Eq. 8, allows to avoid passing through rotation matrices speeding up the computation.

The last considered sensor is the IMU, whose output is the spacecraft angular velocity in the IMU reference frame $\boldsymbol{\omega}_{IMU}^{IMU}(q,t)$ given by Eq. 9 considering the effect of a constant bias, Angular Random Walk (ARW) and Rate Random Walk (RRW).

$$\boldsymbol{\omega}_{IMU}^{IMU} = \mathbf{R}_{B2IMU}(q)\boldsymbol{\omega} + \boldsymbol{\omega}_{bias} + \boldsymbol{\omega}_{ARW} + \boldsymbol{\omega}_{RRW} \tag{9}$$

4.3 Actuator models

Three actuator models are included in the LUMIO ADCS simualtions: Reaction Wheels (RW), Main Engine (ME), and Reaction Control System (RCS). The RW model simulates the wheel dynamics. Appending the angular momentum of each of the four wheels in the vector $\mathbf{h}_{RW} = [h_{RW1}, h_{RW3}, h_{RW3}, h_{RW4}]^{\mathrm{T}}$ and considering the assembly configuration matrix $\boldsymbol{A}_{RW}$, the torque generate by the RW set, $\mathbf{u}_{RW}$, can be expressed as:

$$\mathbf{u}_{RW} = -\left(\boldsymbol{A}_{RW}\dot{\mathbf{h}}_{RW} + \boldsymbol{\omega} \times \boldsymbol{A}_{RW}\mathbf{h}_{RW}\right). \tag{10}$$

The torque $\dot{\mathbf{h}}_{RW}$ imposed on the assembly depends on the mode in which the RW are used, two operative modes are defined in the simulator: nominal and desaturation. In nominal mode the derivative is a function of the ideal control $\mathbf{u}_{id}$ provided as input to the model:

$$\dot{\mathbf{h}}_{RW} = \boldsymbol{A}_{RW}^{*}\left(-\mathbf{u}_{id} + \boldsymbol{A}_{RW}\mathbf{h}_{RW} \times \hat{\boldsymbol{\omega}}(\boldsymbol{\omega}_{IMU}^{IMU})\right). \tag{11}$$

In Eq. 11, $\boldsymbol{A}_{RW}^{*}$ is the pseudo-inverse matrix of $\boldsymbol{A}_{RW}$ and $\hat{\boldsymbol{\omega}}$ is the angular velocity estimated on-board processing the IMU reading. In desaturation mode instead, $\mathbf{h}_{RW}$ is dumped to zero with a proportional control law, see Eq. 12, in which the coefficient k_{desat} is tuned to achieve desaturation within a desired time.

$$\dot{\mathbf{h}}_{RW} = -k_{desat}\mathbf{h}_{RW}. \tag{12}$$

The main engine system is modeled as a blow down thruster with uncertainty on magnitude and firing direction. Referring to Fig. 5 the thrust $\mathbf{F}_{ME}$ produced by the engine and expressed in the ME reference frame is given by:

$$\boldsymbol{F}_{ME}^{ME} = F_n(t-t_0)\left(1+m_\epsilon\right)\begin{bmatrix} \sin(\delta)\cos(\theta) \\ \sin(\delta)\sin(\theta) \\ \cos(\delta) \end{bmatrix}. \tag{13}$$

In Eq. 13, $F_n(t-t_0)$ is the nominal magnitude of the thrust as a function of the firing time given by a blow down curve, $m_\epsilon \sim \mathcal{N}(0,\sigma_m)$ is the magnitude error, $\alpha \sim \mathcal{N}(0,\sigma_d)$ and $\theta \sim \mathcal{U}(-\pi,\pi)$ define the misalignment error. Because of the misalignment between the firing direction and the spacecraft center of mass (CoM), a parasitic torque proportional to the displacement $\mathbf{r}_{CoM2ME}$ is also generated every time that the main engine is activated, as shown in Eq. 14.

$$\mathbf{T}_{par} = \mathbf{r}_{CoM2ME} \times \boldsymbol{F}_{ME} \tag{14}$$

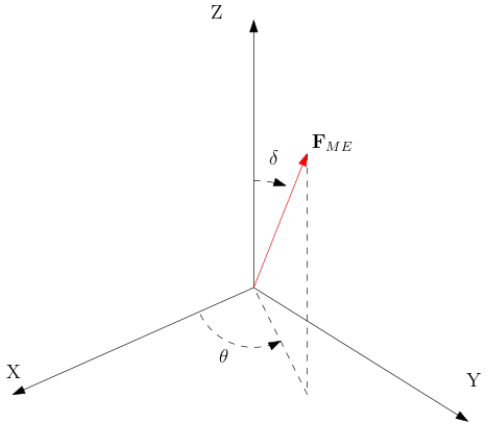

Fig. 5: Thrust direction in the ME reference frame.

Finally, the RCS system is modeled as a simple function that takes as input a vector of boolean flags, each one associated with the status of a single thruster (active or not), and returns the generated torque in body frame $\mathbf{T}_{RCS}$:

$$\mathbf{T}_{RCS} = \mathbf{T}(\boldsymbol{\gamma}_{RCS}, \mathbf{r}_{CoM2RCS})\boldsymbol{u}_{on/off} \tag{15}$$

The complexity of this model lies within the definition of the configuration matrix $\mathbf{T}$ that depends on a series of design parameters embedded in the $\boldsymbol{\gamma}_{RCS}$ and on the CoM displacment. $\boldsymbol{\gamma}_{RCS} = [\alpha, \beta, L, W, F_{RCS}]$ contains a set of geometrical parameters, summarized by Fig. 4, and the thrust F_{RCS} generated from a single nozzle. The total impulse I_{tot} associated with an RCS firing is computed integrating the RCS thrust over all the activated nozzles for the duration of the firing:

$$I_{tot} = \sum_{j=1}^{n_z} \int_{t_0}^{t} \mathbf{F}_{RCS} \left(\boldsymbol{u}_{on/off}\right)_j d\tau \tag{16}$$

A set of control laws is defined to mimic the performance of the ADCS system translating sensors output in actuation commands. This is explained case by case in the following section showing the simulation results.

5 ADCS Analyses

This section presents the ADCS analyses conducted in the context of the Phase B study. As mentioned before, the objective of these analyses is to demonstrate the suitability of the selected components in terms of sizing and configuration.

5.1 Detumbling

The detumbling manoeuvre has to reduce the spacecraft rotations rate after initial deployment. For LUMIO, the spacecraft is considered to be detumbled when the rotation rate on each body axis is below the ST working limit of 1.5 deg/s. The detumbling control law is

$$\mathbf{u}_{id} = -k_1 \mathbf{J}\boldsymbol{\omega}_{IMU} - k_2 \int_{t_0}^{t} \mathbf{J}\boldsymbol{\omega}_{IMU} d\tau \tag{17}$$

where k_1 and k_2 are tuning constants. The integral term compensates the drift in the IMU-estimated angular rates. Because of system considerations, detumbling is executed using the RWs. The latter must be able to deal with tip off rates as high as 10 deg/s on each body axis, and to complete the detumbling manoeuvre in less than 20 minutes. A Monte Carlo (MC) analysis has been carried out to verify the system compliance. To gather statistical results, 1000 simulations have been executed with different initial conditions and IMU noise parameters. The resulting angular rates are reported in Fig. 6, which shows that the spacecraft can be detumbled within the desired amount of time.

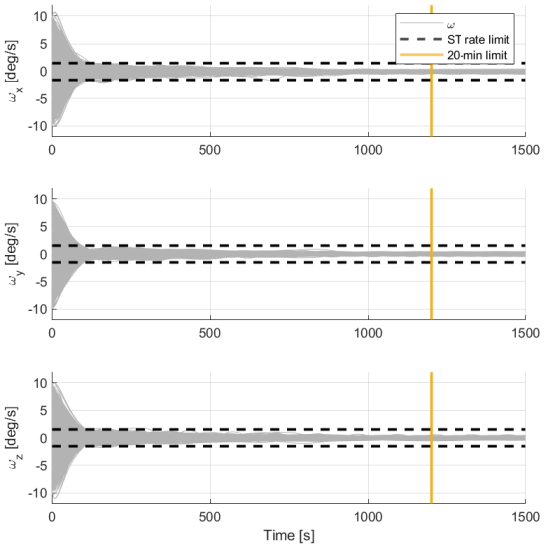

Fig. 6: Angular rates for the detumbling Monte Carlo analysis.

5.2 Pointing budget

The LUMIO mission requires challenging pointing requirements to properly track the Moon and acquire the impact images. The pointing performances of the spacecraft are affected by several Pointing Error Sources (PES) which, coupled together, generate the overall pointing error of the spacecraft. Concerning the LUMIO mission, a major focus is the evaluation of the pointing

accuracy of the LUMIO-Cam during the science phase. To evaluate this error a pointing budget has been evaluated considering several contributions. The most relevant PES arise from the ADCS, the misalignment of the star tracker and the payload during the platform integration, thermoelastic distortion and the orbit determination error. Indeed, the ADCS produce several PES such as the attitude knowledge error, the control algorithms error, the RWs configuration uncertainty, noise, and jitter. Thermoelastic distortions have been evaluated with a system level thermoelastic structural analysis which evaluated the expected displacements on the star tracker and payload lenses in different thermal hot cases expected during the mission. Finally, the position knowledge error is considered in accordance with the orbit determination tolerances and the satellite trajectory during the operative phase of the mission. In the context of the preliminary design of the LUMIO mission all these PES were evaluated and summed to represent a worst-case scenario. The pointing budget of LUMIO estimates an APE of the less than 0.2 degrees, ensuring the payload pointing requirements in a 3-sigma confidence level.

5.3 Main PS parasitic torque compensation

The compensation of the parasitic torque generated during orbital manoeuvres by the main PS is a critical task for the ADCS. Indeed, the 1 N maximum thrust of the main PS is significantly higher than that of the RCS thrusters. Furthermore, the amount of RCS propellant available is strictly limited by volume constraints, which translate into a strict limit on the total impulse available for RCS firings.

The control law used during the main PS firing relies on a phase space controller based on the logic described in [10]. First, an error quaternion is defined which represents the current spacecraft attitude with respect to the desired one for the orbital manoeuvre. This quaternion is then converted to a Gibbs vector to obtain a minimal representation of the attitude error. Differently from [10], instead of using directly the spacecraft angular rates the phase space controller employs the Gibbs vector derivatives, given by:

$$\dot{\mathbf{g}}_e = \frac{1}{2}\left(\hat{\boldsymbol{\omega}} - \hat{\boldsymbol{\omega}} \times \mathbf{g}_e + (\hat{\boldsymbol{\omega}} \cdot \mathbf{g}_e)\mathbf{g}_e\right) \tag{18}$$

where $\mathbf{g}_e$ is the Gibbs vector for the attitude error. A separate phase plane is considered for each of the body axes. Three tuning parameters (g^*, $\dot{g}^*$, $\dot{g}_d$) define the quiescent region, in which the RCS thrusters are not fired. If outside of this region, a positive or negative torque about that axis is requested in order to move towards the origin of the phase plane. The requested torques are stored in a vector $\mathbf{u}_{req}$. The control logic is reported in Alg. 1.

Algorithm 1 RCS thrusters activation logic for parasitic torque compensation.

Given: $\mathbf{g}$, $\dot{\mathbf{g}}$, g^*, $\dot{g}^*$, $\dot{g}_d$
$g_d \leftarrow (\dot{g}_d + \dot{g}^*)\frac{g^*}{\dot{g}^*}$
$\dot{g}_{do} \leftarrow \dot{g}_d + 2\dot{g}^*$
for $i = 1, 2, 3$ **do** ▷ Iterations over body axes
  $u_i \leftarrow 0$
  if $g_i \geq g_d$ **then** ▷ g_i is the i-th component of $\mathbf{g}_e$
    if $\dot{g}_i \geq \dot{g}_d$ **then**
      $u_i \leftarrow -1$
    else if $\dot{g}_i \leq -\dot{g}_{do}$ **then**
      $u_i \leftarrow 1$
    end if
  else if $g_i \leq -g_d$ **then**
    if $\dot{g}_i \leq \dot{g}_d$ **then**
      $u_i \leftarrow 1$
    else if $\dot{g}_i \geq \dot{g}_{do}$ **then**
      $u_i \leftarrow -1$
    end if
  else
    if $\dot{g}_i \geq -\frac{\dot{g}^*}{g^*} g_i + \dot{g}^*$ **then**
      $u_i \leftarrow -1$
    else if $\dot{g}_i \leq -\frac{\dot{g}^*}{g^*} g_i - \dot{g}^*$ **then**
      $u_i \leftarrow 1$
    end if
  end if
end for
$\mathbf{u}_{req} \leftarrow [u_1, u_2, u_3]$

If torque about at least one axis is requested, the vector $\mathbf{u}_{req}$ is then used to decide which RCS thrusters to fire, by minimizing the difference between the direction of the provided torque and that of the desired one:

$$\min_{\mathbf{u}_{on/off}} \left\| \frac{\boldsymbol{T}\mathbf{u}_{on/off}}{\|\boldsymbol{T}\mathbf{u}_{on/off}\|} - \frac{u_{req}}{\|u_{req}\|} \right\| \tag{19}$$

where $\boldsymbol{T}$ is the RCS torque matrix and $\mathbf{u}_{on/off}$ is a boolean vector denoting which RCS thrusters are switched on. Note that RCS thrusters are always fired in couples so that the produced torque is mostly about one spacecraft axis.

The capability of the RCS to counteract the parasitic torque generated by the ME has been evaluated with a MC analysis. The torque generated by the ME depends on the ME thrust, computed with Eq. 13, and the displacement between the geometrical centre of the spacecraft and its centre of mass (CoM). System requirements constrain the center of mass position to a cylinder around the geometrical centre, with a radius of 10 mm and a total height of 30 mm. The constraint is illustrated in Fig. 7, together with the spacecraft body axes as a reference. The position of the CoM can then be defined according to a set of cylindrical coordinates: r_{CoM}, z_{CoM},

θ_{CoM}. For the MC analysis these coordinates are defined as random variables according to the following distributions: $r_{CoM} \sim \mathcal{U}(0, 10)$ mm, $z_{CoM} \sim \mathcal{U}(-15, 15)$ mm, $\theta_{CoM} \sim \mathcal{U}(-\pi, \pi)$. Furthermore, the parameters defining the ME thrust (Eq. 13) also vary randomly, with $\sigma_m = 0.0203$ and $\sigma_d = 0.167°$.

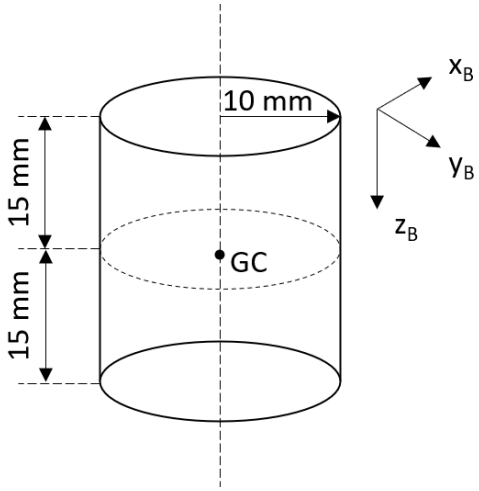

Fig. 7: Cylinder containing the possible centre of mass positions.

The MC analysis is carried out considering 500 samples. All the possible firing time of the ME is simulated, which amounts to slightly more than 90 minutes. Fig. 8 shows the histogram of the total impulse required by the RCS to compensate the parasitic torque throughout the firing. The distribution has its peak below 100 Ns, but it is significantly skewed towards higher values. The sample mean is 106.50 Ns, the minimum is 50.92 Ns, the maximum is 203.36 Ns and the 95th percentile is 170.48 Ns. The latter is the value that will later be used for the computation of the RCS total impulse required for the mission. Fig. 9 illustrates the absolute pointing error (APE) over the 500 simulations during the ME firing. As the ME is a blowdown system, its thrust, and consequently the parasitic torque, decreases over time. Initially, when the thrust is at its max value, part of the samples are slightly above the desired 0.5° error value. As the thrust decreases, the error does too. From about 20 minutes on, all the samples are within the desired limit, except for a few sporadic peaks. Selecting more stringent tuning parameters for the phase space controller described above could reduce the maximum APE, but would increase the required total impulse. Since the latter is limited by system constraints, it is preferred to keep the configuration as it is, given that this does not represent a criticality for the mission. Indeed, mission analyses have shown that the spacecraft is robust to significantly higher angular errors during orbital manoeuvres, up to 1.5°, 1-sigma, meaning that requirement ADC.033 could be safely relaxed.

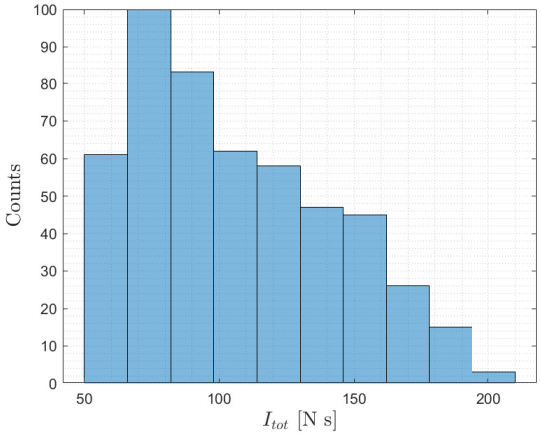

Fig. 8: Histogram of the total impulse required to compensate the main engine parasitic torque.

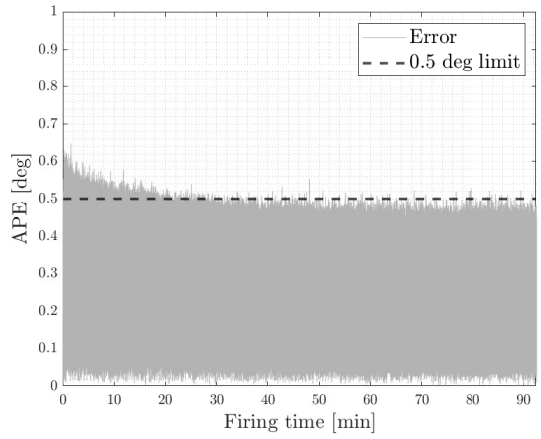

Fig. 9: Absolute pointing error during main engine firing.

5.4 *Reaction wheel desaturation*

The objective of desaturation is to bring the angular momentum of the reaction wheel from an initial state $\mathbf{h}_{RW,0}$ to zero without tumbling the spacecraft, i.e. keeping $\boldsymbol{\omega} \leq \boldsymbol{\omega}_{lim}$. Desaturation is achieved imposing the dumping profile of Eq. 12 and compensating the generated torque given by Eq. 10 using the RCS. This has to be achieved in consideration of the total impulse limitation of the system of 230 N s. To assess the inital desaturation condition a momentum budget is required

in different operative scenarios. Three cases are considered:

1. A reference WSB transfer arc lasting 120 days.
2. A full Nav&Eng + Science cycle on the operative orbit (30 Days).
3. A worst-case scenario for detumbling.

Since the detumbling analysis is already discussed in Sec. 5.1, only the first two cases are reported here and shown in Fig. 10 and Fig. 11.

For the transfer case a nominal pointing profile is selected with the primary pointing towards Earth and the secondary pointing such that the panels' exposure to the Sun is maximized. In particular, given the Earth and the Sun direction in body frame $\hat{\mathbf{r}}_E$, $\hat{\mathbf{r}}_S$ the Direction Cosine Matrix defining the spacecraft attitude is given by:

$$R_{N2B} = \begin{bmatrix} \dfrac{\hat{\mathbf{r}}_E \times \hat{\mathbf{r}}_S}{\|\hat{\mathbf{r}}_E \times \hat{\mathbf{r}}_S\|} \times \hat{\mathbf{r}}_E \\ \dfrac{\hat{\mathbf{r}}_E \times \hat{\mathbf{r}}_S}{\|\hat{\mathbf{r}}_E \times \hat{\mathbf{r}}_S\|} \\ \hat{\mathbf{r}}_E \end{bmatrix} \tag{20}$$

In a similar way for the operative phase on the halo orbit a Moon pointing is adopted, see Eq. 21, with the only difference that periodically a slew to Earth for telecom or a random pointing for manoeuvering is commanded.

$$R_{N2B} = \begin{bmatrix} \dfrac{\hat{\mathbf{r}}_M \times \hat{\mathbf{r}}_S}{\|\hat{\mathbf{r}}_M \times \hat{\mathbf{r}}_S\|} \times \hat{\mathbf{r}}_M \\ \dfrac{\hat{\mathbf{r}}_M \times \hat{\mathbf{r}}_S}{\|\hat{\mathbf{r}}_M \times \hat{\mathbf{r}}_S\|} \\ \hat{\mathbf{r}}_M \end{bmatrix} \tag{21}$$

Simulations within CUBORG have been performed to assess the momentum budget on the different mission phases. As an example, Fig. 10 shows the evolution of RW momentum in time during the full Nav&Eng + Science cycle. This analysis concluded that only one desaturation is required per orbit to remove residual stored momemtum before staring a new operational cycle. It is worth noting that slew manoeuvres executed during the operational orbit do not lead to the accumulation of angular momentum, since the spacecraft quickly returns to the nominal pointing conditions.

Similar simulations have been performed for the WSB transfer arc, leading to the conclusion that two desaturation maneuvers are required during this phase. Therefore, a breakdown of the transfer momentum budget is performed assuming a first manoeuvre after 75 days (where the peak of stored momentum is reached) and a second one at the end of the transfer to clean out residual momentum before operative phase. Furthermore, a desaturation manoeuvre is assumed to be performed immediately after detumbling. For the latter, a conservative case is analysed, which considers all the RWs fully saturated. Tab. 2 summarizes the initial conditions adopted for the analysis.

Tab. 2: Initial conditions for the desaturation analysis.

Phase	$\boldsymbol{h}_{RW,0}$ **[mN m s]**
Transfer 1	$[-1.4197, -90.3133, 11.5973, 46.2663]^T$
Transfer 2	$[20.4197, 3.4334, -13.4990, -5.9713]^T$
Halo	$[-13, -10, 17, 4]^T$
Detumbling	$[100, 100, 100, -50]^T$

The control law $\mathbf{u}_{on/off}(t)$ used to operate the RCS and compensate the parasitic torque is the result of an actuator fitting process in which the following optimal control problem is solved:

$$\min_{\mathbf{u}_{on/off}(t)} \|\boldsymbol{T}\mathbf{u}_{on/off}(t) - k\hat{\boldsymbol{\omega}}\| \tag{22}$$

with

$$\textstyle\sum_j^{n_z} \left(\boldsymbol{u}_{on/off}\right)_j = 0 \quad \text{or} \quad \sum_j^{n_z} \left(\boldsymbol{u}_{on/off}\right)_j = 2 \tag{23}$$

The second constraint is used to make sure that only appropriate couples of RCS thrusters are fired together. Fig. 12 and Fig. 13 show an example of the desaturation profiles, reporting the angular momentum decay of the RW and the angular velocity of the spacecraft, together with the bounds of $\boldsymbol{\omega}_{lim}$.

The results of the desaturation analysis are reported in Tab 3, indicating for each phase the allocated total impulse.

Tab. 3: Total impulse budget for desaturation manoeuvres.

Phase	I_{tot} **[N s]**
Transfer 1	3.9
Transfer 2	0.27
Halo	1.6
Detumbling	3.5

5.5 RCS total impulse

The RCS total impulse is directly linked to the amount of available propellant. Given the tight volume constraints on the spacecraft, a strict limit of 230 Ns is set for the total impulse, which must consider all RCS operations. The required total impulse is computed by considering the analyses described in Sec. 5.3 and Sec. 5.4. However, while the former considers a detailed statistical analysis, the latter does not provide statistical information on the uncertainty distribution of the total impulse required for desaturation. For this reason a margin of 100% is applied to the values reported in Tab. 3 when computing

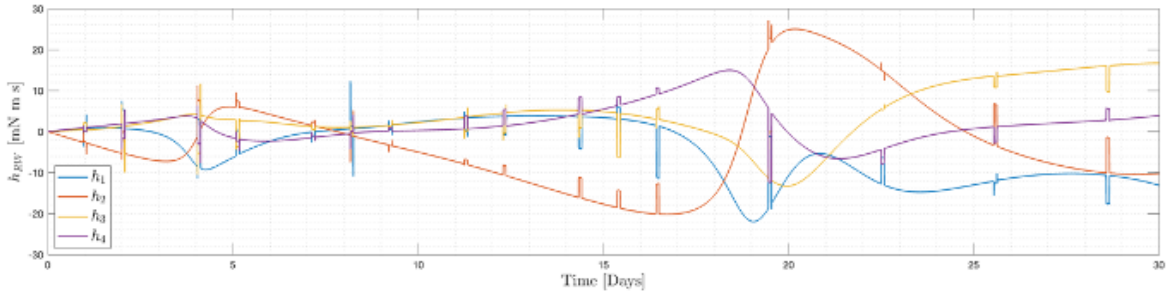

Fig. 10: Momentum budget during the operational orbit.

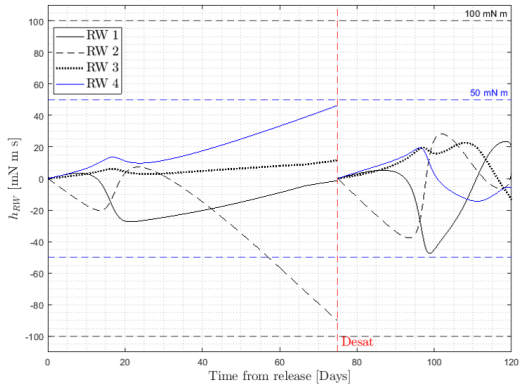

Fig. 11: Momentum budget during transfer.

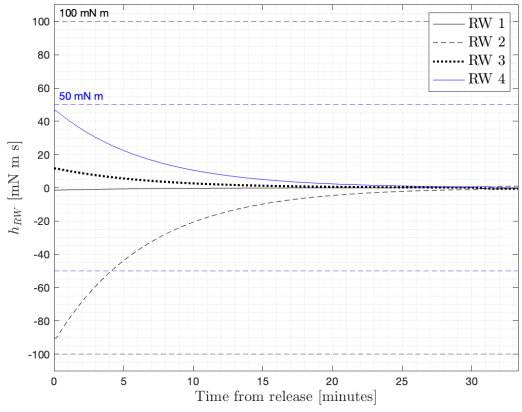

Fig. 12: RW angular momentum during desaturation - transfer case.

the total impulse. Considering a mission lifetime of 12 months the total impulse can be computed as:

$$I_{tot} = I_{Mis}^{95\%} + 2(I_{Transfer} + 12I_{Halo} + I_{Detumbling}) = 224 \text{ N s} \quad (24)$$

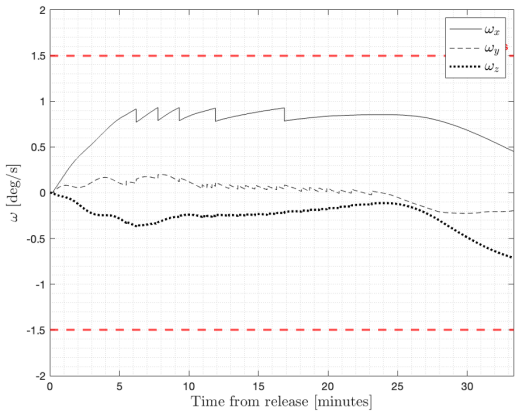

Fig. 13: Angular velocity profile during desaturation - transfer case.

where $I_{Mis}^{95\%}$ is the 95th percentile of the distribution in Fig. 8. This result shows compliance with the 230 N s limit imposed by the requirements.

6 Conclusion

This paper presented the LUMIO ADCS status at the end of Phase B. The current configuration of the AOCS has been described, together with the relevant requirements and the analyses conducted to validate the system design. Despite the significant limitations derived from the CubeSat platform, especially in terms of volume constraints, the analyses have shown that the current design of the ADCS suits the needs of the LUMIO mission. In particular, the main criticality for the ADCS design is the limited volume available for RCS propellant tanks, which constrains the available RCS total impulse. Therefore, detailed analyses have been conducted to estimate the amount of RCS total impulse required during the mission. By far, the main contribution to the total impulse is the compensation of the main PS parasitic

torque. Therefore, this contribution has been evaluated with a statistical analysis, demonstrating that the RCS can safely compensate the main PS torque.

Future work will evaluate in more detail the pointing performance of the system, both in terms of APE and RPE. Preliminary results show that the selected components can provide the required accuracy. These will be complemented by detailed analyses in the next phases to verify in detail the associated requirements.

Bibliography

[1] Z. Ceplecha, J. Borovička, W. G. Elford, D. O. ReVelle, R. L. Hawkes, V. Porubčan, and M. Šimek. Meteor phenomena and bodies. *Space Science Reviews*, 84(3):327–471, 1998. doi:10.1023/A:1005069928850.

[2] A. Cervone, F. Topputo, S. Speretta, A. Menicucci, E. Turan, P. Di Lizia, M. Massari, V. Franzese, C. Giordano, G. Merisio, D. Labate, G. Pilato, E. Costa, E. Bertels, A. Thorvaldsen, A. Kukharenka, J. Vennekens, and R. Walker. LUMIO: A CubeSat for observing and characterizing micro-meteoroid impacts on the Lunar far side. *Acta Astronautica*, 195:309–317, 2022. doi:10.1016/j.actaastro.2022.03.032.

[3] F. Topputo, G. Merisio, V. Franzese, C. Giordano, M. Massari, G. Pilato, D. Labate, A. Cervone, S. Speretta, A. Menicucci, E. Turan, E. Bertels, J. Vennekens, R. Walker, and D. Koschny. Meteoroids detection with the LUMIO lunar CubeSat. *Icarus*, 389:115213, 2023. doi:10.1016/j.icarus.2022.115213.

[4] G. Merisio and F. Topputo. Present-day model of lunar meteoroids and their impact flashes for LUMIO mission. *Icarus*, 389:115180, 2023. doi:10.1016/j.icarus.2022.115180.

[5] P. Panicucci, F. Piccolo, S. Borgia, A. Rizza, V. Franzese, and F. Topputo. Current status of the lumio autonomous optical navigation experiment. In *12th International Conference on Guidance, Navigation & Control Systems (GNC)*, pages 1–15, 2023.

[6] L. Provinciali, F. Topputo, V. Franzese, G. Saita, L. Bozzoli, A. Pipino, G. Fumo, L. Pattanaro, A. Balossino, and L. Conterio. Lumio mission: Observation and characterization of lunar meteoroid impact. In *74th International Astronautical Congress (IAC 2023)*, 2023.

[7] A. M. Cipriano, D. A. Dei Tos, and F. Topputo. Orbit design for LUMIO: The lunar meteoroid impacts observer. *Frontiers in Astronomy and Space Sciences*, 5:29, 2018. doi:10.3389/fspas.2018.00029.

[8] A Rizza, F Piccolo, M Pugliatti, P Panicucci, and F Topputo. Hardware-in-the-loop simulation framework for cubesats proximity operations: Application to the milani mission. In *73rd International Astronautical Congress (IAC 2022)*, pages 1–15, 2022.

[9] Bong Wie. *Space vehicle dynamics and control*. Aiaa, 1998.

[10] Brandon C Stiltner, Benjamin Diedrich, Christopher Becker, Ivan Bertaska, Andy F Heaton, and Juan Orphee. Cold gas reaction control system for the near earth asteroid scout cubesat. In *AIAA SPACE and Astronautics Forum and Exposition*, page 5185, 2017.